Article

A Robust Adaptive Extended Kalman Filter Based on an Improved Measurement Noise Covariance Matrix for the Monitoring and Isolation of Abnormal Disturbances in GNSS/INS Vehicle Navigation

Zhihui Yin [1], Jichao Yang [2,*], Yue Ma [1,3], Shengli Wang [2,4], Dashuai Chai [5] and Haonan Cui [2]

1   College of Geodesy and Geomatics, Shandong University of Science and Technology, Qingdao 266590, China
2   College of Ocean Science and Engineering, Shandong University of Science and Technology, Qingdao 266590, China
3   College of Electronic Information, Wuhan University, Wuhan 430072, China
4   Key Laboratory of Ocean Geomatics, Ministry of Natural Resources, Qingdao 266590, China
5   College of Surveying and Geo-informatics, Shandong Jianzhu University, Jinan 250101, China
*   Correspondence: yangjichao@sdust.edu.cn

Abstract: Global Navigation Satellite Systems (GNSS) integrated with Inertial Navigation Systems (INS) have been widely applied in many Intelligent Transport Systems. However, due to the influence of various factors, such as complex urban environments, etc., accurately describing the measurement noise statistics of GNSS receivers and inertial sensors is difficult. An inaccurate definition of the measurement noise covariance matrix will lead to the rapid divergence of the position error of the integrated navigation system. To overcome this problem, this paper proposed a Robust Adaptive Extended Kalman Filter (RAKF) method based on an improved measurement noise covariance matrix. By analyzing and considering the position accuracy factors, measurement factor, and position standard deviation in GNSS measurement results, this paper constructed the optimal measurement noise covariance matrix. Based on the Huber model, this paper constructed a two-stage robust adaptive factor expression and obtained the robust adaptive factors with and without abnormal disturbances. And robust adaptive filtering was carried out. To assess the performance of this method, the author conducted experiments on land vehicles by using a self-developed POS system (GNSS/INS combined navigation system). The classic Extended Kalman Filter algorithm (EKF), Adaptive Kalman Filter (AKF) algorithm, Robust Kalman Filter (RKF) algorithm, and the proposed method were compared through data processing. Experimental results show that compared with the classical EKF, AKF, and RKF, the positioning accuracies of the proposed method were improved by 72.43%, 2.54%, and 47.82%, respectively, in the vehicle land experiment. In order to further evaluate the performance of this method, the vehicle data were subjected to different times and degrees of disturbance experiments. Experimental results show that compared with EKF, AKF, and RKF, the heading angle accuracy had obvious advantages, and its accuracy was improved by 34.65%, 31.53%, and 18.36%, respectively. Therefore, this method can effectively monitor and isolate disturbance and improve the robustness, reliability, accuracy, and stability of GNSS/INS integrated navigation systems in complex urban environments.

Keywords: GNSS/INS; Robust Adaptive Kalman Filter; Extended Kalman Filter; measurement noise covariance matrix; robust adaptive factor

1. Introduction

Resilient Positioning, Navigation, and Timing (PNT) services are essential elements for ensuring a high-quality life and are fundamental to high-speed rail, aviation, and highway transportation systems [1]. The continuous, robust, and reliable generation of PNT

information forms the core of resilient PNT [2]. Therefore, the monitoring and isolation of abnormal disturbances in aviation, marine, and land vehicles is one of the important means to improve the accuracy, reliability, and stability of navigation and positioning results.

GNSS are widely used for positioning and navigation in aviation, maritime, and land vehicle applications [3–7]. However, due to complex environmental factors [8], adverse weather conditions, and multipath effects, GNSS measurements often contain disturbances (see Figure 1a) [9]. Relying solely on GNSS positioning is challenging to meet the integrity and reliability requirements for land vehicle navigation [10]. Inertial Navigation Systems (INS) are independent systems immune to external environmental interference [11]. However, INS errors gradually accumulate over time [12], and the Inertial Measurement Unit (IMU) data may also contain outliers due to road vibrations and other factors, as illustrated in Figure 1b. Therefore, in order to achieve more accurate navigation and positioning results, the method of integrating GNSS and INS is commonly used [13]. However, during the measurement process, when GNSS measurements are affected by disturbances, reliable position measurements cannot be obtained, resulting in abnormal updates of the measurement results and rapid divergence of the integrated navigation system's positioning solution [14]. Therefore, when GNSS measurements are disturbed, how to effectively fuse GNSS and INS in a combined navigation system and ensure its normal operation is an urgent issue.
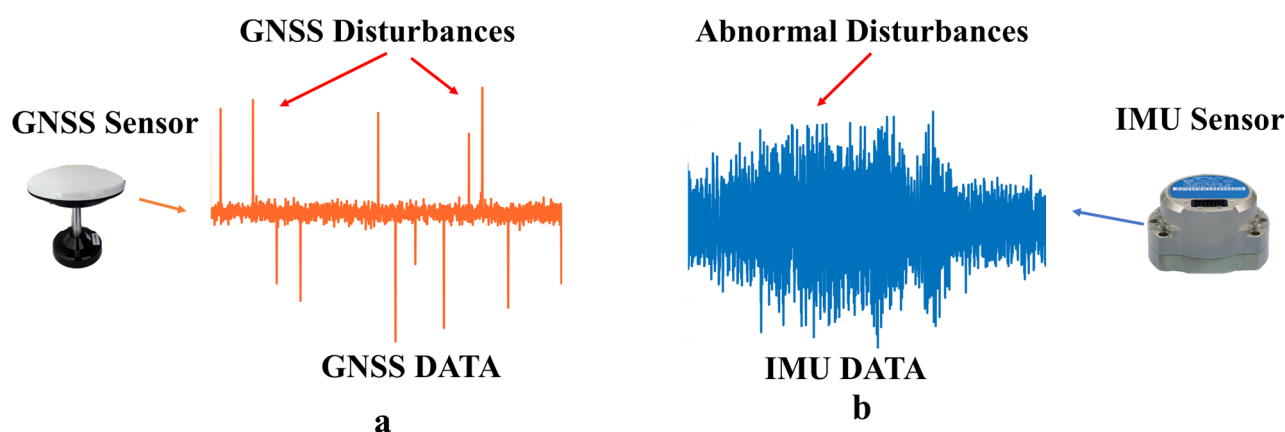
Figure 1. GNSS, IMU disturbances. (**a**) GNSS sensor; (**b**) IMU sensor.

The Kalman filter [15] is a commonly used method for fusing GNSS and INS data [16]. However, the performance of KF relies on the accurate definition of the stochastic and state models [17]. The stochastic model describes the random characteristics of the system process and measurement noises, and the state model describes the state change in the system state with time [18]. The uncertainty in the covariance matrices of the system process and measurement noises significantly affects the performance of the Kalman filter [19]. Typically, determining the system process and measurement noises covariance matrices requires good empirical analysis, and in practice, the system process and measurement noises covariance matrices are often fixed and lack flexibility [18]. Over the past decades, significant research has been conducted on robust Kalman filtering [20] and adaptive filtering algorithms [21] to mitigate the impact of inaccurately defined system processes and measurement noises. Adaptive stochastic models include residual-based adaptive models [22] and covariance-based adaptive models [23], which estimate the covariance matrices of the system process and measurement noises directly, monitor the changes in the covariance of innovations and residuals, and make timely adjustments. Hide et al. [24] developed a covariance scaling approach to improve filter stability by introducing scaling factors in the covariance matrix. Meng et al. [25] estimated the covariance of process and measurement noises by maintaining consistency between the numerical values of innovations or residual covariances and theoretical values. Yang et al. [26] adaptively adjusted the weights of the

prediction parameters based on the difference between the system measurements and the predicted innovations, combining robust maximum likelihood estimation with adaptive filtering. Gao et al. [27] developed a robust adaptive filter that adaptively adjusts the covariance matrix of the system state noise based on an adaptive factor constructed from the prediction residuals.

Due to previous studies, the GNSS positioning error estimates, usually represented by variance or standard deviation, have been used to determine the measurement noise covariance matrix in GNSS/INS integrated navigation Kalman filters, thereby influencing the integrated navigation results [28]. However, in challenging environments such as urban complex environments or poor road conditions, there exists significant inconsistency between the estimated error from GNSS solutions and the actual GNSS positioning error [29]. Furthermore, previous research has mainly focused on detecting and mitigating GNSS disturbances to minimize their impact on GNSS/INS integrated navigation systems, while less attention has been given to the monitoring and isolation of abnormal disturbances in the remaining GNSS measurement result data. Therefore, this paper primarily investigates the construction method of an improved measurement noise covariance matrix R and a robust adaptive factor ϖ, aiming to effectively monitor and isolate abnormal disturbance, thereby enhancing the robustness, reliability, accuracy, and stability of GNSS/INS integrated navigation systems in complex urban environments or adverse road conditions. This method utilizes different combinations of Position Dilution of Precision (**PDOP**), measurement factors (**Q**), and position mean square deviation to construct the measurement noise covariance matrix, and employs the Huber method [30] to generate the robust adaptive factor based on the normalized residuals, achieving robust adaptive filtering.

The structure of this paper is as follows: Section 2 overviews the proposed method. This section presents the overall framework and process of the improved robust adaptive algorithm based on the construction of the measurement noise covariance matrix and introduces the construction of the improved measurement noise covariance matrix for robust adaptive filtering experiments and obtains the optimal measurement noise covariance matrix R and robust adaptive factor ϖ. Section 3 validates the performance of the proposed method through vehicle experiments and experiments with different durations and levels of disturbances. Section 4 discusses the results of the experiment. Finally, Section 5 concludes this paper.

2. Materials and Methods

2.1. Steps of the Improved Robust Adaptive Factor Method

The framework of the Robust Adaptive Kalman Filter (RAKF) based on the construction of an improved measurement noise covariance matrix is depicted in Figure 2. The algorithm consists of four main modules: (1) the formulation of state measurement equations and state update equations; (2) the construction of the improved measurement noise covariance matrix; (3) the construction of the robust adaptive factor ϖ, and (4) the implementation of the robust adaptive filtering algorithm.

(1) The module for constructing the state measurement equations and state update equations involves formulating the state equation and measurement equation using the position, velocity, and attitude information obtained from INS and the position and velocity information obtained from GNSS. These equations are essential for performing the state update process in the Kalman filter.

(2) The module for constructing the improved measurement noise covariance matrix R involves creating the covariance matrix of measurement noise using the Position Dilution of Precision (**PDOP**), the measurement factor **Q**, and the standard deviation of position (STD). Through experimental analysis with different values of parameters a and b, the relative optimal results are obtained to determine the best measurement noise factors a and b.
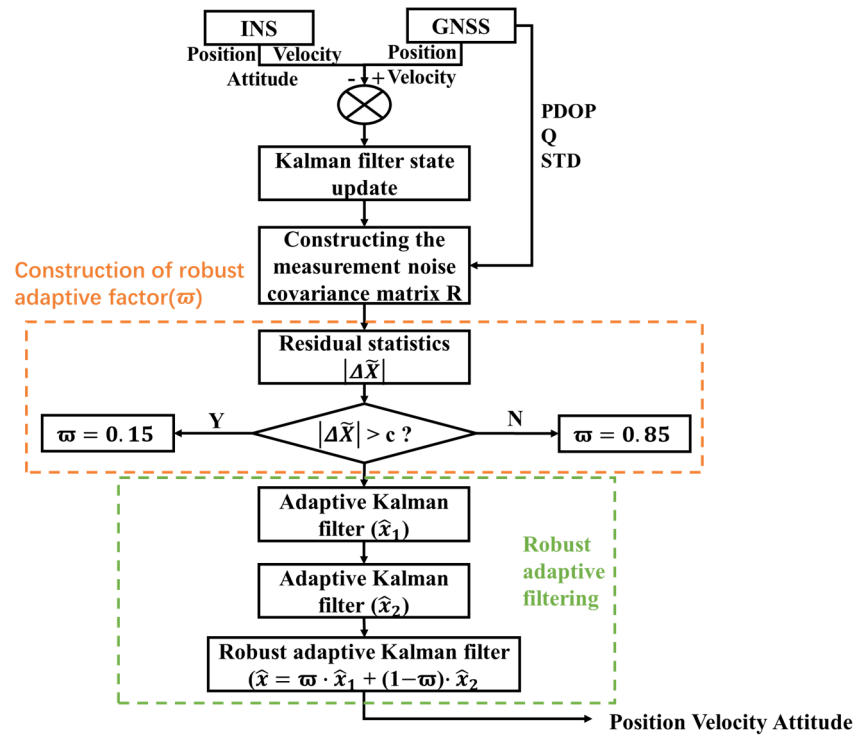
Figure 2. A GNSS/INS vehicle anomalous disturbance monitoring and isolation flowchart based on an improved measurement noise covariance matrix with anti-differential adaptive filtering.

(3) The module for constructing the robust adaptive factor ϖ involves evaluating the standardized residuals and comparing their magnitude with a predefined constant. Adaptive filtering can automatically adjust the parameters of the filter under different dynamic conditions to adapt to changes in the system [31]. Robust filtering can maintain the stability of the estimation in the face of abnormal disturbances and improve the reliability of navigation [31]. The value of the robust adaptive factor is mainly based on the empirical value. We set the robust adaptive factor under normal conditions to 0.85. That is, the weight of the integrated navigation result obtained by adaptive filtering is set to 0.85, and considering the combination of the results of adaptive filtering and robust filtering, the sum of the weight of adaptive filtering and the weight of robust filtering should be 1, so the weight of robust filtering is set to 0.15.

(4) The module for robust adaptive filtering involves performing both adaptive Kalman filtering and robust Kalman filtering separately. The results obtained from these two filters are then combined using the robust adaptive factor, which assigns different weights to each filter's output. Ultimately, the robust adaptive filtering result is obtained by incorporating these weighted outputs. Finally, the feasibility of the algorithm is verified by using measured onboard data, and the effectiveness of the algorithm is further verified by adding different numerical perturbations for different time lengths.

2.2. Classical GNSS/INS Loosely Coupled Integrated Procedure

In this paper, we used an Extended Kalman Filter [32] GNSS/INS loose combination model with a 21-dimensional state volume and a 3-dimensional volume measure.

The state equations and measurement equations for the GNSS/INS integrated navigation system can be formulated as follows [33]:

$$\delta \dot{x}(t) = F(t)\delta x(t) + G(t)w(t) \tag{1}$$

$$Z_k = H_k X_k + v_k \tag{2}$$

In the equation, $F(t)$ represents the system's state transition matrix, $G(t)$ denotes the system's dynamic noise matrix, $w(t)$ represents the process noise white noise vector of the system, and $\delta x(t)$ represents the state vector of the 21 unknown parameters, Z_k represents the measurement vector, $Z_k = \begin{bmatrix} \delta r_N & \delta r_E & \delta r_D \end{bmatrix}^T$, H_k represents the measurement matrix, and v_k represents the measurement noise matrix.

The state vector is [34]:

$$\delta x(t) = \left[\left(\delta r_{INS}^n \right)^T \quad \left(\delta v_{INS}^n \right)^T \quad \phi^T \quad b_g^T \quad b_a^T \quad s_g^T \quad s_a^T \right]^T \tag{3}$$

In the equation, δr_{INS}^n represents the position error of INS, δv_{INS}^n represents the velocity error of INS, ϕ represents the attitude error of INS, b_g denotes the gyroscope bias, b_a denotes the accelerometer bias, s_g denotes the gyroscope scale factor error, and s_a denotes the accelerometer scale factor error.

The measurement matrix H_k for the position measurement values is defined as follows:

$$H_k = \begin{bmatrix} I_3 & 0_3 & \left(C_b^n l_{GNSS}^b \times \right) & 0_3 & 0_3 & 0_3 & 0_3 \end{bmatrix} \tag{4}$$

In the equation, l^b represents the lever arm, and I represents the identity matrix.

2.3. Robust Adaptive Filtering Algorithm with Improved Measurement Noise Covariance Matrix

The basic idea of constructing an improved measurement noise covariance matrix robust adaptive filtering algorithm in this paper is as follows: First, the optimal measurement noise covariance matrix is obtained by considering different combinations of *PDOP*, *Q*, and position STD square. Second, adaptive filtering and robust filtering are employed to calculate the robust adaptive factor ϖ based on the magnitude of the residual statistics. Finally, the adaptive filtering results and the robust filtering results are combined using different robust adaptive factors to obtain the robust adaptive filtering results. The flowchart of the improved measurement noise covariance matrix adaptive robust filtering process is illustrated in Figure 3.
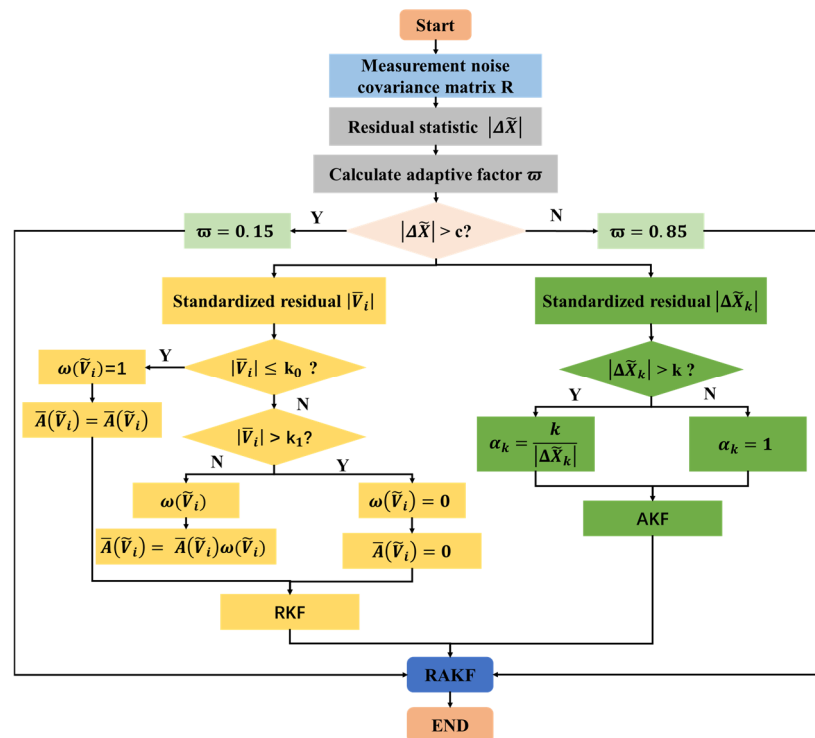

Figure 3. A flowchart for constructing the improved robust adaptive filtering of measurement noise covariance matrix.

2.3.1. Construction of the Improved Measurement Noise Covariance Matrix

Since the measurement noise statistics in the measurement process of the GNSS/INS integrated navigation system are unknown, how to define the measurement noise statistics is very important to the performance of the Kalman filter. And the GNSS positioning error estimates, usually represented by an experience value or variance [28], have been used to determine the measurement noise covariance matrix in GNSS/INS integrated navigation Kalman filters in the previous studies. However, in challenging environments, such as urban complex environments or poor road conditions, there exists significant inconsistency between the estimated error from GNSS solutions and the actual GNSS positioning error [29]. Therefore, this article, through considering a comprehensive analysis of *PDOP* (Position Dilution of Precision), *Q*, and the standard deviation of the North, East, and Down positions, determined the measurement noise covariance matrix R as follows:

$$R = PDOP^a Q^b r^2 \tag{5}$$

In the equation, ^{a} denotes the number of *PDOP*, and ^{b} denotes the number of *Q*. And *r* denotes the STD value of the position in the North, East, and Down directions. The Position Dilution of Precision (*PDOP*) in the equation is a dimensionless factor that represents the favorable extent of satellite geometry on the accuracy of three-dimensional positioning. When the satellites are evenly distributed in the North, South, East, and West directions, a strong satellite geometry structure occurs, resulting in a lower *PDOP*. *PDOP* values within the range of 1 to 2 indicate excellent satellite geometry shape, while values within 2–3 are considered sufficient in a certain sense as they themselves usually do not limit positioning accuracy. Values between 3 and 4 are regarded as marginal, while values close to or exceeding 5 are considered poor.

The determination of the measurement factor *Q* is based on the values obtained from 3D Accurate and is presented in detail in Table 1.

Table 1. Variation in the measurement factor *Q* values for different 3D accuracies.

Measurement Factor (Q)	Description	3D Accuracy (m)
1	Fixed integer	0.00–0.15
2	Converged float or noise Fixed integer	0.05–0.40
3	Converging float	0.2–1.0
4	Converging float	0.5–2.00
5	DGPS	1.00–5.00
6	DGPS	2.00–10.00

2.3.2. Robust Adaptive Filtering Construction

In this paper, when constructing the adaptive factor α_k, the prediction residual method [35] was employed to obtain the statistic, which is defined as follows:

$$\Delta \widetilde{X}_k = \left(\frac{\overline{V}_k^T \overline{V}_k}{tr\left(P_{\overline{V}_k}\right)} \right)^{\frac{1}{2}} \tag{6}$$

In the equation, $\overline{V}_k$ represents residual vector [36] $\overline{V}_k = H_k \hat{X}_k - Z_k$, $\Delta \widetilde{X}_k$ represents residual statistic, $P_{\overline{V}_k}$ represents the covariance matrix of the a priori state vector, which is denoted as $P_{\overline{V}_k} = \Phi_k P_{\hat{X}_{k-1}} \Phi^T + Q_k$.

On this basis, the two-stage method was employed to construct the adaptive factor α_k, which is given by:

$$\alpha_k = \begin{cases} 1 & \left|\Delta \widetilde{X}_k\right| \le k \\ \frac{k}{\left|\Delta \widetilde{X}_k\right|} & \left|\Delta \widetilde{X}_k\right| > k \end{cases} \tag{7}$$

In the formula, k is a constant, generally set to 1.0~1.5. ($k = 1.0$)

- Calculate the gain matrix: $K_{ak} = \frac{1}{\alpha_k} P_{k/k-1} H_k^T (\frac{1}{\alpha_k} H_k P_{k/k-1} H_k^T + R_k)^{-1}$;
- Calculate the state estimate at time k: $\hat{X}_{ak} = \hat{X}_{k/k-1} + K_{ak}(Z_k - H_k \hat{X}_{k/k-1})$;
- Calculate the estimate error covariance matrix at time k: $P_{ak} = \frac{1}{\alpha_k}(I - K_{ak} H_k) P_{k/k-1}$.

By utilizing the state Equation (1) and the measurement Equation (3), the innovation vector $\hat{V}_k$ can be obtained as follows:

$$\hat{V}_k = L_k - H_k \hat{X}_{k/k-1} \tag{8}$$

In the formula, L_k is the observation vector. If the measurement vector at time k, denoted as Z_k, and the predicted state vector $X_{k/k-1}$, both follow contaminated distributions, the extremum condition can be constructed as follows [37]:

$$\Omega = \overline{V}_k^T \overline{A}_k \overline{V}_k + \alpha_k \overline{V}_k^T \overline{A}_{\hat{X}_k} \overline{V}_k = \mathbf{min} \tag{9}$$

where $\overline{A}_k$ is the equivalent weight matrix of the measurement vector Z_k. The weighting function used in this paper was the IGGIII [38] weighting function:

$$\omega\left(\widetilde{V}_i\right) = \begin{cases} 1 & \left|\widetilde{V}_i\right| \le k_0 \\ \frac{k_0}{\left|\widetilde{V}_i\right|} \left(\frac{k_1 - \left|\widetilde{V}_i\right|}{k_1 - k_0}\right)^3 & k_0 < \left|\widetilde{V}_i\right| \le k_1 \\ 0 & \left|\widetilde{V}_i\right| > k_1 \end{cases} \tag{10}$$

From this, the corresponding equivalent weight is:

$$\overline{A}(\widetilde{V}_i) = \begin{cases} \overline{A}(\widetilde{V}_i) & \left|\widetilde{V}_i\right| \le k_0 \\ \overline{A}(\widetilde{V}_i) w(\widetilde{V}_i) & k_0 < \left|\widetilde{V}_i\right| \le k_1 \\ 0 & \left|\widetilde{V}_i\right| > k_1 \end{cases} = \begin{cases} \overline{A}(\widetilde{V}_i) & \left|\widetilde{V}_i\right| \le k_0 \\ \overline{A}(\widetilde{V}_i) \frac{k_0}{\left|\widetilde{V}_i\right|} \left(\frac{k_1 - \left|\widetilde{V}_i\right|}{k_1 - k_0}\right)^3 & k_0 < \left|\widetilde{V}_i\right| \le k_1 \\ 0 & \left|\widetilde{V}_i\right| > k_1 \end{cases} \tag{11}$$

In the formula, $\overline{A}(\widetilde{V}_i) = R_i^{-1}$, $\widetilde{V}_i$ is the standardized residual; k_0 and k_1 are constants, usually selected as $k_0 = 1.0 \sim 1.5$, (In the experiment $k_0 = 1.15$ $k_1 = 4.45$)

- Calculate the gain matrix: $K_{rk} = P_{k/k-1} H_k^T (H_k P_{k/k-1} H_k^T + \overline{A}_k^{-1})^{-1}$;
- Calculate the state estimate at time k: $\hat{X}_{rk} = \hat{X}_{k/k-1} + K_{rk}(Z_k - H_k \hat{X}_{k/k-1})$;
- Calculate the estimate error covariance matrix at time k: $P_{rk} = (I - K_{rk} H_k) P_{k/k-1}$.

Based on the adaptive filtering results obtained from $\hat{X}_{ak}$ and the robust Kalman filtering results obtained from $\hat{X}_{rk}$, the combined robust Kalman filtering result $\hat{X}_k$ is obtained as follows $\hat{X}_k$:

$$\hat{X}_k = \varpi * \hat{X}_{ak} + (1 - \varpi) * \hat{X}_{rk} \tag{12}$$

The covariance matrix corresponding to the state estimation $\hat{X}_k$ is:

$$P_k = \varpi * P_{ak} + (1 - \varpi) * P_{rk} \tag{13}$$

The Huber model was used to construct the robust adaptive factor ϖ according to Equation (13):

$$\varpi = \begin{cases} 0.85 & \left|\Delta\widetilde{X}_k\right| \le c \\ 0.15 & \left|\Delta\widetilde{X}_k\right| > c \end{cases} \tag{14}$$

In the formula, c is a constant ($c = 1.0$).

2.4. Datasets and Processing Strategies

In this paper, we mounted a self-developed POS and the SPAN-LCI tactical-grade fiber optic inertial guidance systems on the same vehicle to collect two different sets of INS data. The GNSS data acquisition equipment used the Novatel OEM718D GNSS receiver with a data-sampling frequency of 5 Hz, and the configuration of Novatel commands is shown in Figure 4. And this paper used three global satellite systems: the Global Positioning System (GPS), the Global Navigation Satellite System (GLONASS), and the BeiDou Navigation Satellite System (BDS), in the Novatel OEM718D GNSS receiver. The data-sampling frequency was 100 Hz for the self-developed POS system and 200 Hz for the SPAN-LCI tactical-grade fiber optic inertial guidance system. The data were collected from 06:22:00 to 06:48:28 on 28 April 2022 and lasted approximately 30 min. The experiment used a single antenna model.
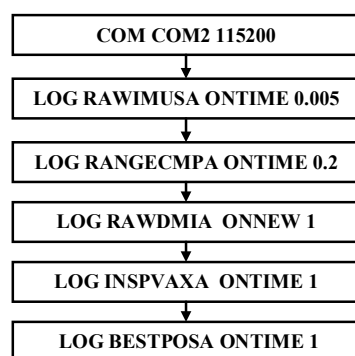

Figure 4. The configuration of Novatel commands.

The device parameters of the self-research POS system using inertial sensors are shown in Table 2.

Table 2. Navigation and positioning sensor parameters.

	Gyroscopes	Accelerometers
Bias	0.25°/h	0.025°/h
Random noise	0.04°/sqrt(h)	0.03m/s/sqrt(h)

The GNSS reference station was set up on the roof of the School of Marine Science and Engineering of the Shandong University of Science and Technology, with open and unobstructed surroundings, and the mobile station was mounted on the car. The experimental equipment was fixed to the car to form the mobile station. In order to avoid human interference factors, a route was determined so the equipment could accept data normally. The carrier exacted a figure 8-type large corner movement, with the trajectory around the Shandong University of Science and Technology constituting a rectangle. The experimental equipment was installed, as shown in Figure 5. The trajectory is shown in Figure 6.

Figure 5. Experimental car and sensors.

Figure 6. Trajectories of the experiments on land. (① and ② denote the trajectories corresponding to the occurrence of anomalous perturbations.)

3. Results

3.1. Experimental Results for the Measurement Noise Covariance Matrix

The numerical values of the measurement noise covariance matrix R were set as presented in Table 3.

Table 3. Setting different values for the measurement noise covariance matrix.

Method	R
1	$R = r^2$
2	$R = pdop*Q*r^2$
3	$R = pdop*r^2$
4	$R = pdop^2*Q*r^2$
5	$R = pdop^3*Q*r^2$
6	$R = pdop^2*Q^2*r^2$
7	$R = pdop^2*Q^3*r^2$

Figure 7 illustrates the variations in the measurement noise covariance matrix R obtained from the experiment.

Figure 7 illustrates the variations in the diagonal elements of the measurement noise covariance matrix R for different selected values. The numbers 1–7 indicate that RAKF takes different R values, and 1–7 correspond to the value of R in Table 3. It can be observed from Table 4 that significant changes in the position standard deviation occurred around 400 s, 800 s, and 1000 s. The results of different R values during the experiment are shown in Table 4.

Taking into consideration the different combinations of measurement noise covariance matrices as shown in Table 3 and the results presented in Table 4, a comparison of the Extended Kalman Filter (EKF) with mode 4 demonstrates improvements of 26.65%, 77.92%, and 72.56% in the positioning accuracy of East, North, and Up directions, respectively, for method 4. When compared with mode 2 and while maintaining similar positioning, velocity, and attitude accuracies, the accuracy of upward velocity is improved by 25.76%. Compared with mode 3, the position accuracy in the upward direction is improved by 4.91%. Compared with mode 5, the accuracy of the position in the upward direction is increased by 21.89%, and the velocity in the upward direction is increased by 30.70%. Compared with mode 6, the position accuracy in the upward direction is improved by 17.13%. Compared with mode 7, the position accuracy in the upward direction is improved by 20.54%. Therefore, considering the positioning errors, velocity errors as well as attitude errors, the optimal choice is to select the measurement noise factor with [a] = 2 and [b] = 1, resulting in the measurement noise covariance matrix denoted as $R = PDOP^2 * Q * r^2$.
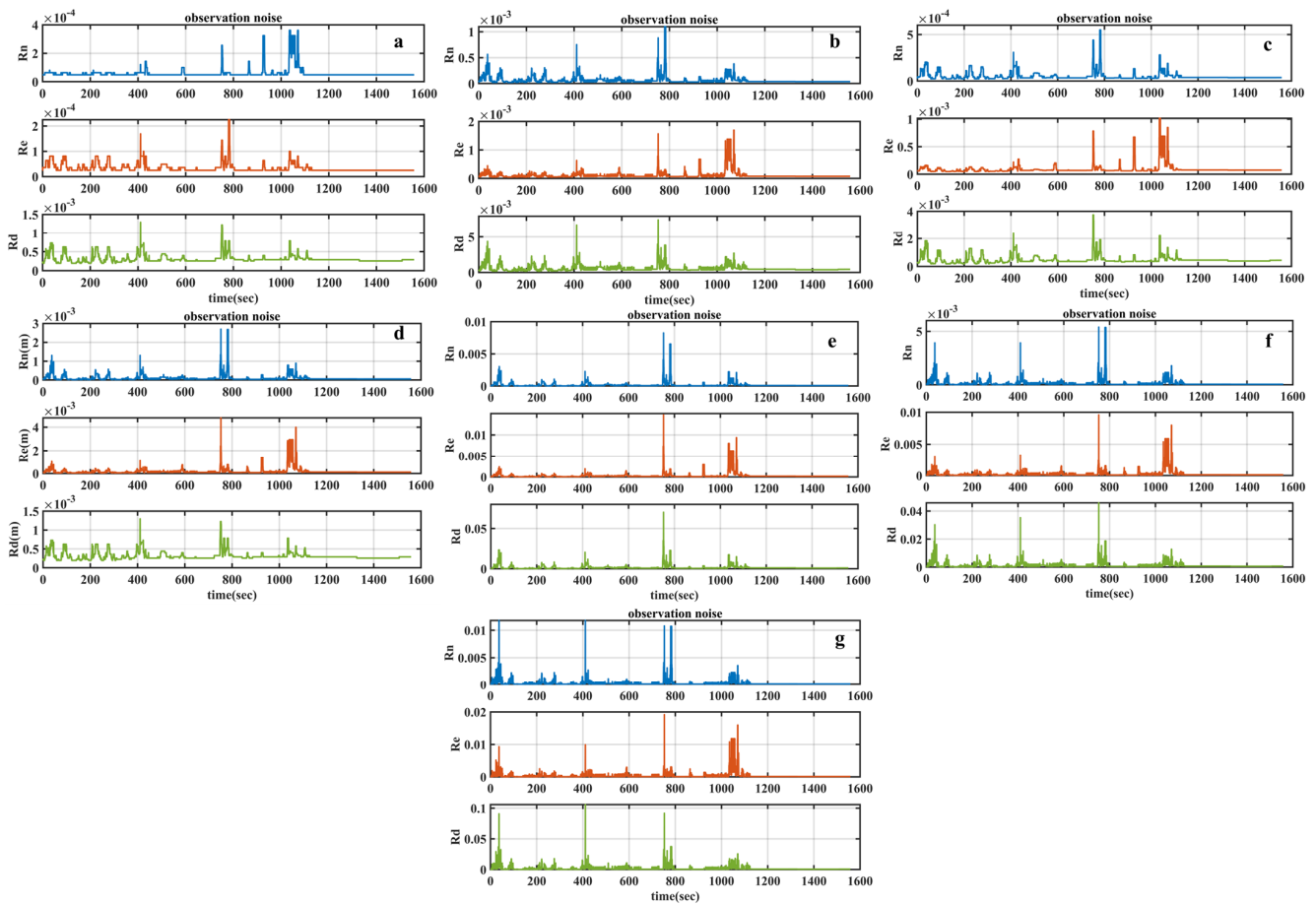
Figure 7. Variations in the R values for the measurement noise covariance matrix. (**a**) the change of R = r^2; (**b**) the change of R = pdop*Q*r^2; (**c**) the change of R = pdop*r^2; (**d**) the change of R = pdop^2*Q*r^2, (**e**) the change of R = pdop^3*Q*r^2, (**f**) the change of R = pdop^2*Q^2*r^2, (**g**) the change of R = pdop^2*Q^3*r^2.

Table 4. Different measurement noise covariance matrices to obtain the corresponding RMS values of the navigation results.

| Mode	P_E (m)	P_N (m)	P_U (m)	V_E (m/s)	V_N (m/s)	V_U (m/s)	Pitch (°)	Roll (°)	Yaw (°)
EKF	0.0703	0.2867	0.1833	0.0718	0.4025	0.0991	0.3230	0.2136	0.3824
1	0.0509	0.0632	0.0508	0.0482	0.0555	0.1001	0.1287	0.1404	0.2514
2	0.0514	0.0632	0.0542	0.0486	0.0558	0.0982	0.1301	0.1378	0.2453
3	0.0512	0.0631	0.0529	0.0484	0.0557	0.0729	0.1307	0.1408	0.2453
4	**0.0513**	**0.0633**	**0.0503**	**0.0493**	**0.0562**	**0.0729**	**0.1307**	**0.1408**	**0.2409**
5	0.0531	0.0639	0.0644	0.0497	0.0566	0.1052	0.1307	0.1377	0.2409
6	0.0520	0.0635	0.0607	0.0494	0.0563	0.0743	0.1295	0.1445	0.2406
7	0.0521	0.0638	0.0633	0.0495	0.0565	0.0793	0.1298	0.1419	0.2396
Improved (%)	26.65%	77.92%	72.56%	31.34%	86.04%	26.44%	59.54%	33.57%	37.00%

3.2. Vehicle Experimental Results

3.2.1. Vehicle Experimental 1 Results

The loosely coupled integration of DGNSS/INS was realized by robust adaptive filtering software using the observation noise covariance matrix from experiment 3.1. Four different schemes were designed for this dataset: Method 1 utilized the Extended Kalman Filter (EKF) [39], Method 2 employed the Adaptive Kalman Filter (AKF) [40], Method 3 employed the Robust Kalman Filter (RKF) [39], and Method 4 was based on the

proposed Robust Adaptive Filtering with Measurement Noise Covariance Matrix (RAKF). The high-precision navigation solution obtained through the tightly coupled integration of GNSS/INS and post-processing smoothing was used as a reference ground truth.

The four different methods were implemented using custom software, and the resulting position and velocity errors in the East (E), North (N), and Up (U) directions are shown in Figure 8.
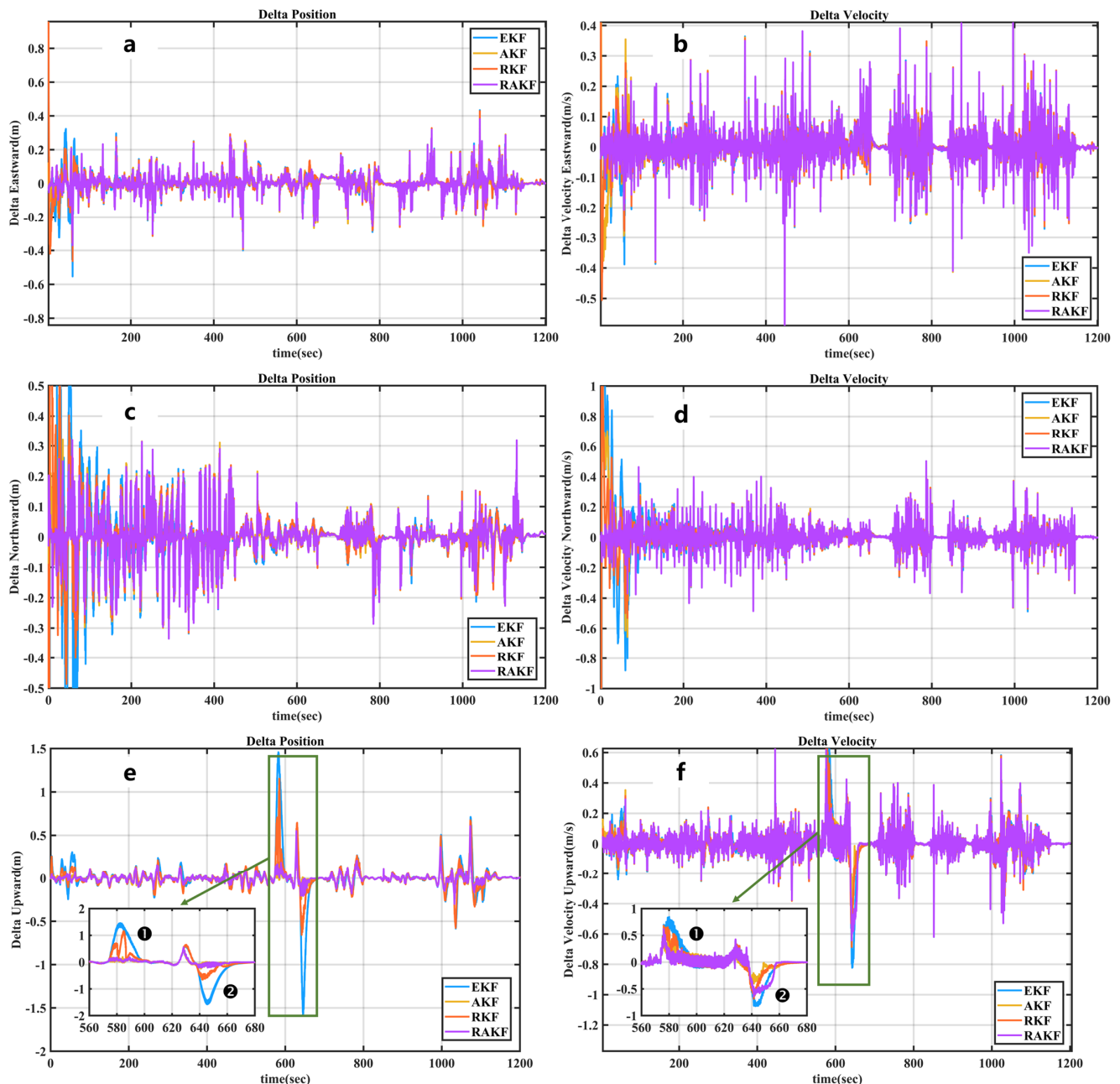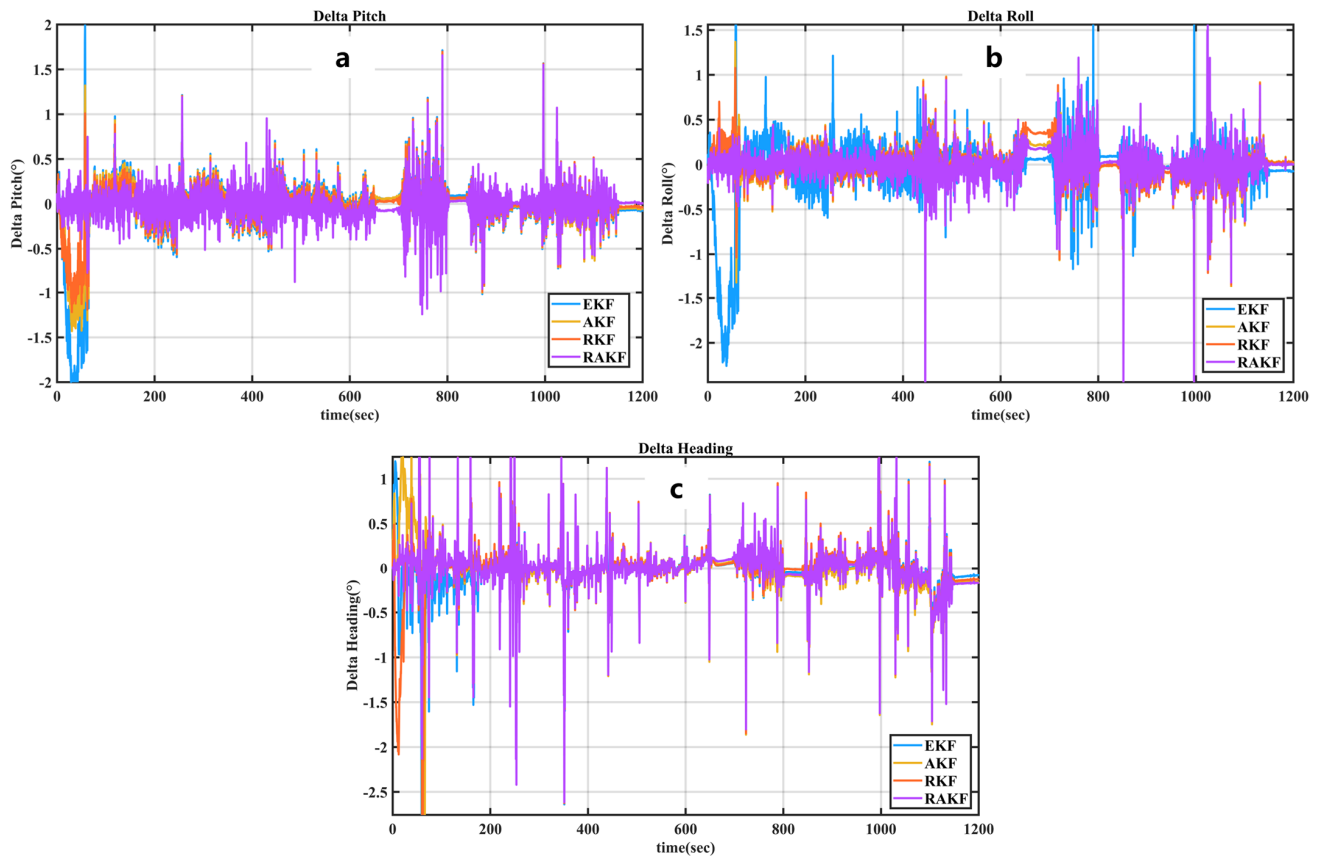

Figure 8. Comparison of position velocity error. (**a**) Eastward position error; (**b**) eastward velocity error; (**c**) northward position error; (**d**) northward velocity error; (**e**) upward position error; (**f**) upward velocity error.

Figure 8 represents a comparison of position and velocity errors in the East, North, and Up directions. Figure 8a,c,e illustrate the comparison of position errors in the East, North, and Up directions. Figure 8b,d,f depict the comparison of velocity errors in the East, North, and Up directions, respectively. Notably, in Figure 8e,f, the velocity and position errors exhibit significant variations around 600 s in the Up direction. To further analyze

this, we zoomed in on the intervals 560–600 s and 620–660 s, corresponding to markers ① and ② in Figure 6. It is evident that among the four approaches, RAKF showed smaller variations in errors and was closer to zero.

Further investigation was conducted to examine the error variations in attitude for the four approaches. The resulting attitude errors in the roll, pitch, and heading directions are depicted in Figure 9.


Figure 9. Comparison of attitude angle error. (**a**) Pitch error; (**b**) roll error; (**c**) heading error.

In order to further compare the position, velocity, and attitude accuracy of the four schemes, the root mean square (RMS) of position and velocity errors were plotted in a histogram, as shown in Figure 10. The corresponding results are summarized in Table 5.

Table 5. Position velocity attitude RMS.

	ERROR	**EKF**	**AKF**	**RKF**	**RAKF**
Velocity (m/s)	Eastward	0.0718	0.0750	0.0700	0.0493
	Northward	0.4025	0.2507	0.2797	0.0562
	Upward	0.0991	0.0623	0.0751	0.0729
Attitude (deg)	Pitch	0.3230	0.2250	0.1931	0.1307
	Roll	0.2136	0.1608	0.1667	0.1408
	Heading	0.3824	0.3650	0.3061	0.2453
Position (m)	Eastward	0.0703	0.0528	0.0663	0.0513
	Northward	0.2867	0.0710	0.1313	0.0633
	Upward	0.1833	0.0428	0.1098	0.0503
	3D Accuracy(m)	0.3475	0.0983	0.1836	0.0958
	improved accuracy (%)	72.43%	2.54%	47.82%	
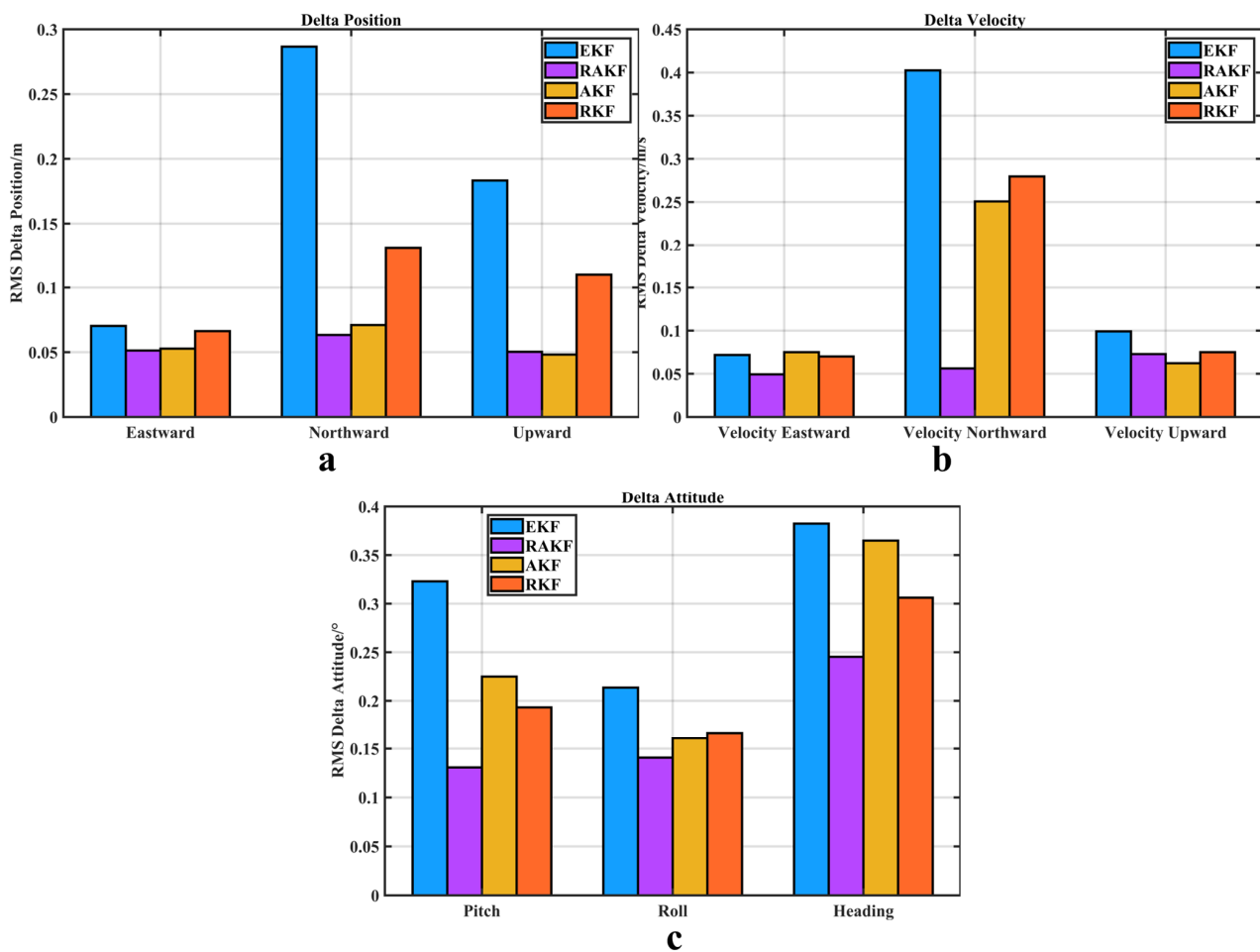
Figure 10. Position velocity and attitude error RMS value. (**a**) Position error RMS; (**b**) velocity error RMS; (**c**) attitude error RMS.

Table 5 presents the RMS values of position, velocity, and attitude errors. Based on the results in Table 5, the following conclusions can be drawn:

- Regarding position error: In terms of the East–North–Up (ENU) position error, compared with EKF, the accuracy of RAKF increased by 27.03%, 77.92%, and 72.56%, respectively. Compared with AKF, the accuracy of RAKF improved by 2.84% and 10.85%, respectively. Compared with RKF, the accuracy of RAKF improved by 22.62%, 51.79%, and 54.19%, respectively. In the position average accuracy, compared with the three algorithms, the accuracy of RAKF improved by 72.43%, 2.54%, and 47.82%, respectively.
- Regarding velocity error: In terms of the East–North–Up (NEU) velocity error, compared with EKF, the accuracy of RAKF increased by 31.34%, 86.04%, and 26.44%, respectively. Compared with AKF, the accuracy of RAKF improved by 34.27% and 77.58%, respectively. Compared with RKF, the accuracy of RAKF improved by 29.57%, 79.91%, and 2.93%, respectively.
- Regarding attitude errors: In terms of the pitch–roll–heading–attitude error, compared with EKF, the accuracy of RAKF increased by 59.54%, 34.08%, and 35.85%, respectively. Compared with AKF, the accuracy of RAKF improved by 41.91%, 12.44%, and 32.79%, respectively. Compared with RKF, the accuracy of RAKF improved by 32.31%, 15.54%, and 19.86%, respectively.

3.2.2. The Comparison Results of the Single GPS System and GPS+GLONASS+BDS Three Systems

On the basis of vehicle experiment 1, this paper used the RAKF to test the single GPS system and the GPS+GLONASS+BDS three systems, respectively. The comparison of the

number of satellites between the single GPS system and the GPS+GLONASS+BDS three systems is shown in Figure 11.
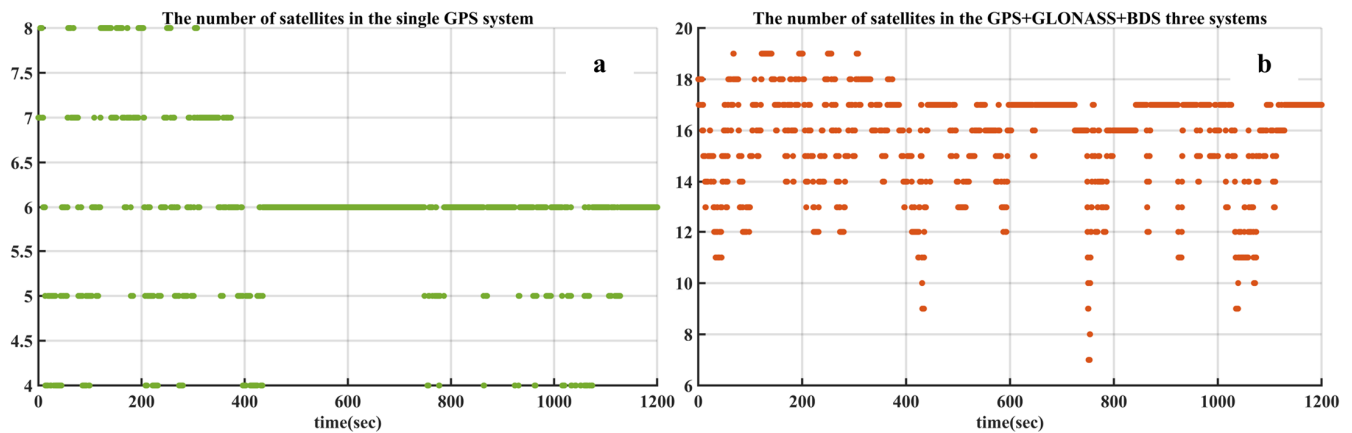
Figure 11. Comparison of the number of satellites between the single GPS system and the GPS+GLONASS+BDS three systems. (**a**) Number of satellites in the single GPS system; (**b**) number of satellites in the GPS+GLONASS+BDS three systems.

The velocity and attitude change was small, so this paper compared the position error. The experimental position results are shown in Figure 12.
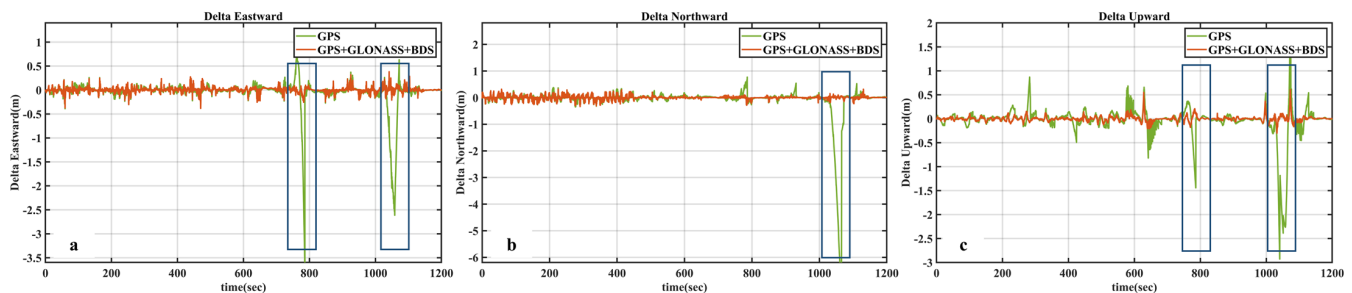
Figure 12. The comparison of position error between the single GPS and the GPS+GLONASS+BDS three systems. (**a**) Eastward position error; (**b**) northward position error; (**c**) upward position error.

The box in Figure 12 showed no GPS satellite when the single GPS was working. And the accuracy of the GPS+GLONASS+BDS three systems was better than that of the single GPS system. This paper used the GPS+GLONASS+BDS three systems in this experiment. The position error results are shown in Table 6.

Table 6. The comparison of position error between the single GPS and the GPS+GLONASS+BDS three systems.

	Eastward Error STD (m)	Northward Error STD (m)	Upward Error STD (m)	3D Accuracy (m)
Single GPS	0.3059	0.5926	0.3148	0.7375
Three systems	0.0521	0.0643	0.0510	0.0972
improved accuracy (%)	82.97%	89.15%	83.80%	86.82%

Compared with the single GPS system, the GPS+GLONASS+BDS three systems in the eastward, northward, and upward increased by 82.97%, 89.15%, and 86.82%, respectively.

3.2.3. Vehicle Experiment 2 Results

On the basis of vehicle experiment 1, the same equipment as vehicle experiment 1 was used for this vehicle experiment 2. The data collection time was from 15:36:00 to 15:54:04

on 4 October 2022. The satellite systems involved in the calculations in this experiment were GPS, GLONASS, and BDS. This experiment used the single antenna model. The experimental trajectory is shown in Figure 13.

Figure 13. Trajectories of experiments on land. The blue point represents the starting point, and the purple point represents the endpoint.
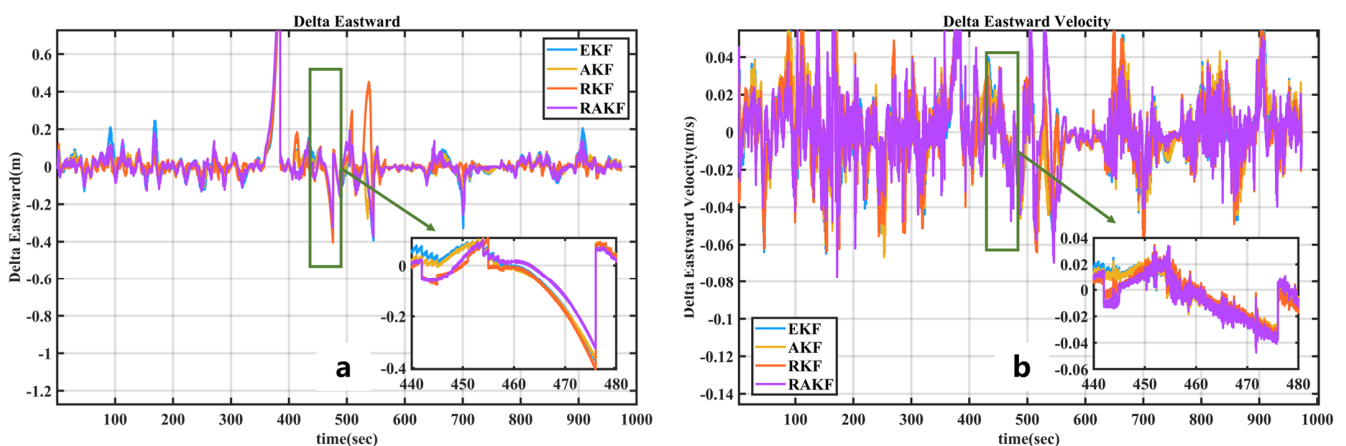
The comparison of position and velocity errors obtained by the four modes is shown in Figure 14.

Further investigation was conducted to examine the error variations in attitude for the four approaches. The resulting attitude errors in the roll, pitch, and heading directions are depicted in Figure 15.

In order to further compare the position, velocity, and attitude accuracy of the four schemes, the root mean square (RMS) of position and velocity errors were plotted in a histogram, as shown in Figure 16. The corresponding results are summarized in Table 7.

Table 7 presents the RMS values of position, velocity, and attitude errors. Based on the results in Table 6, the following conclusions can be drawn:

- Regarding position error: In terms of the East–North–Up (ENU) position error, compared with EKF, the accuracy of RAKF increased by 0%, 66.28%, and 9.53%, respectively. Compared with AKF, the accuracy of RAKF improved by 5.34% and 64.86%, and 3.22%, respectively. Compared with RKF, the accuracy of RAKF improved by 8.24%, 44.23%, and 9.35%, respectively. In the position average accuracy, compared with the three algorithms, the accuracy of RAKF improved by 27.53%, 21.89%, and 15.63%, respectively.
- Regarding velocity error: In terms of the East–North–Up (ENU) velocity error, compared with EKF, the accuracy of RAKF increased by 19.81%, 29.67%, and 20.22%, respectively. Compared with AKF, the accuracy of RAKF improved by 16.16%, 27.82%, and 7.89%, respectively. Compared with RKF, the accuracy of RAKF improved by 14.87%, 16.16%, and 18.21%, respectively.
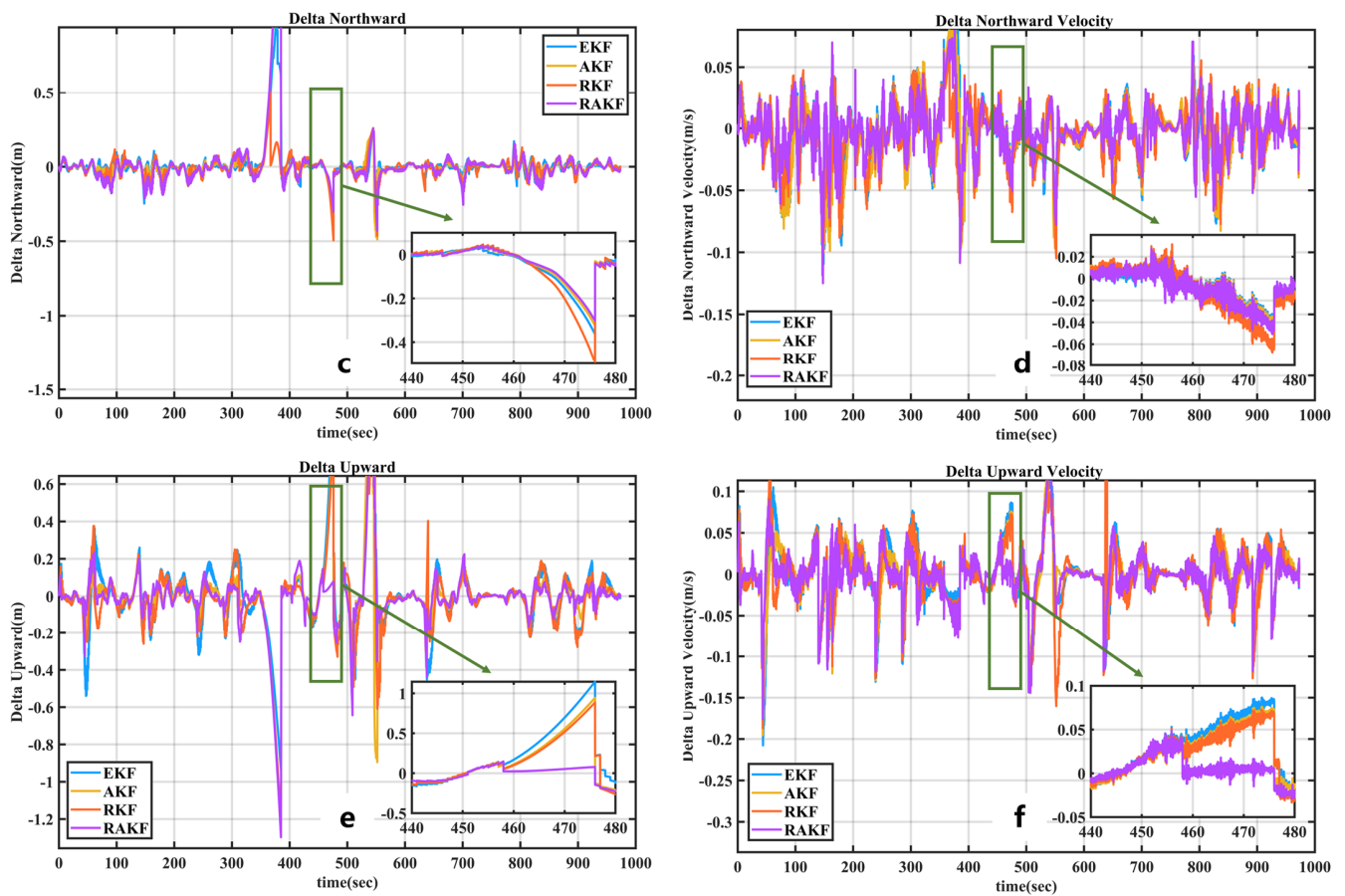

Figure 14. *Cont.*

Figure 14. Comparison of position velocity error. (**a**) Eastward position error; (**b**) eastward velocity error; (**c**) northward position error; (**d**) northward velocity error; (**e**) upward position error; (**f**) upward velocity error.
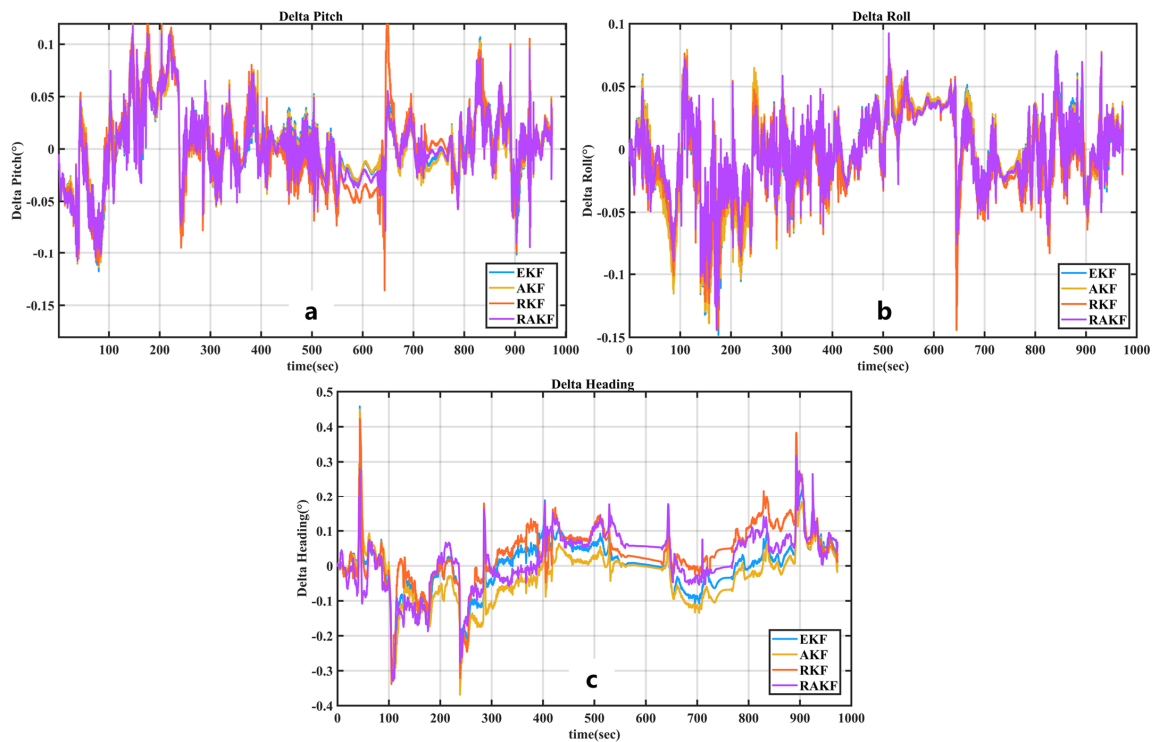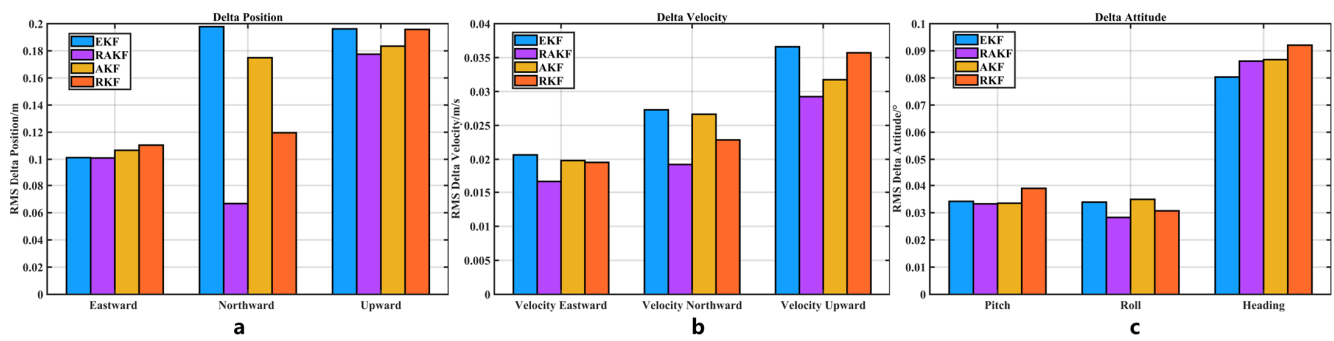

Figure 15. Comparison of attitude angle error. (**a**) Pitch error; (**b**) roll error; (**c**) heading error.

Figure 16. Position velocity and attitude error RMS value. (**a**) Position error RMS; (**b**) velocity error RMS; (**c**) attitude error RMS.

Table 7. Position velocity attitude RMS.

	ERROR	**EKF**	**AKF**	**RKF**	**RAKF**
Velocity (m/s)	Eastward	0.0207	0.0198	0.0195	0.0166
	Northward	0.0273	0.0266	0.0229	0.0192
	Upward	0.0366	0.0292	0.0317	0.0357
Attitude (deg)	Pitch	0.0342	0.0335	0.0389	0.0333
	Roll	0.0339	0.0349	0.0307	0.0283
	Heading	0.0803	0.0868	0.0921	0.0862
Position (m)	Eastward	0.1013	0.1067	0.1104	0.1010
	Northward	0.1978	0.1749	0.1196	0.0667
	Upward	0.1962	0.1834	0.1958	0.1775
	3D Accuracy(m)	0.2964	0.2750	0.2546	0.2148
	improved accuracy (%)	27.53%	21.89%	15.63%	

3.3. Add Different Disturbance Vehicle Experiment Results

To further validate the effectiveness of the proposed algorithm, additional experiments were conducted by artificially introducing gross errors on top of the aforementioned vehicular experiments. The experiments were divided into two groups:

Group 1: Within a one-second interval centered around GPST 368,963 s, random errors ranging from 0 to 1 were added.

Group 2: Within a five-second interval from GPST 369,398 s to 369,402 s, specific perturbations of 0.2721 m, 1.0997 m, 1.1594 m, 0.3380 m, and 0.2899 m were added. The details are presented in Table 8.

Table 8. Adding the length and value of different perturbations.

Experimental	Add Perturbation Time/s	Add Perturbation Value/m	Disturbance Duration/s
Group 1	368963	0.1576 0.9706 0.9572 0.4854 0.8003	1
Group 2	369398	0.2721	1
	369399	1.0997	1
	369400	1.1594	1
	369401	0.3380	1
	369402	0.2899	1

Due to the possibility of the ***PDOP*** values and the standard deviation of the position in the East, North, and Up directions remaining unchanged in the presence of perturbations or gross errors, this study set the ***PDOP*** and position standard deviation values to be constant when introducing perturbations. Based on different 3D accuracy values, the ***Q*** values for the first group of experiments at GPST 368963s were set to 2, 3, 3, 3, and 3, respectively. For the second group of experiments, the ***Q*** values at GPST 369,398 s, 369,399 s, 369,400 s, 369,401 s, and 369,402 s were set to 2, 4, 4, 2, and 2, respectively.

3.3.1. Experimental Results of the First Group

Figure 17 shows the comparison of position, velocity, and attitude errors in the presence of randomly added errors ranging from 0 to 1 during the 1-s interval at GPST 368,963 s. The figure also includes localized zoomed-in error plots for the time interval from 368,942 s to 368,947 s, which contained the one-second interval with added perturbations. The purpose of these plots is to observe the performance comparison of the four different algorithms under the presence of perturbations.
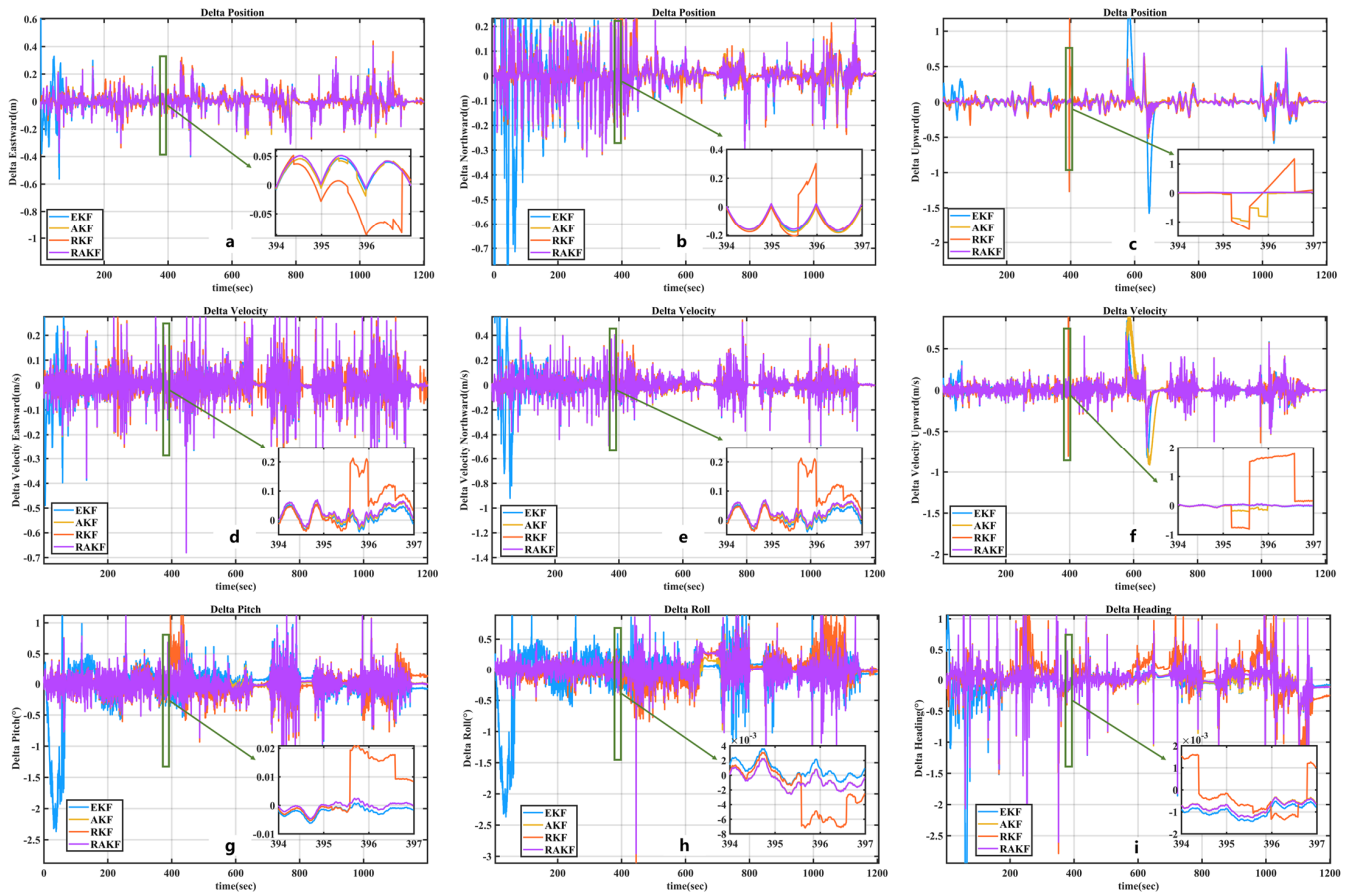
Figure 17. One-second perturbation position, velocity, and attitude error result diagrams. (**a**) Eastward position error; (**b**) northward position error; (**c**) upward position error; (**d**) eastward velocity error; (**e**) northward velocity error; (**f**) upward velocity error; (**g**) pitch error; (**h**) roll error; (**i**) heading error.

Figure 17 represents the plots of position, velocity, and attitude errors obtained by adding a 1-s perturbation at GPST 368,963 s. Figure 17a–c illustrate the position error plots in the East, North, and Up directions. Figure 17d–f show the velocity error plots in the East, North, and Up directions. Figure 17g–i display the attitude error plots for pitch, roll, and heading angles. Furthermore, an analysis of the overall error RMS histogram and the error RMS values, as shown in Figure 18 and in Table 9, was conducted to further examine the effects of the 1-s perturbation.
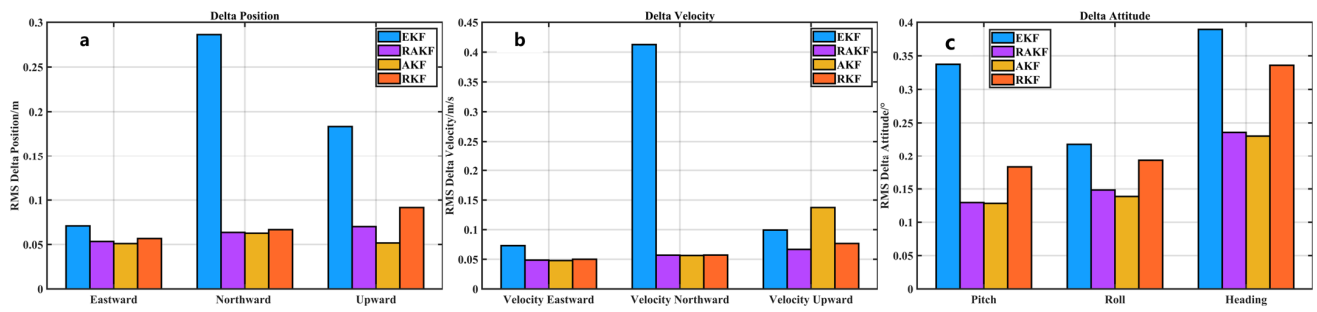
Figure 18. Comparison of RMS values of position, velocity, and attitude errors under 1-s disturbance. (**a**) Position error RMS; (**b**) velocity error RMS; (**c**) attitude error RMS.

Table 9. Adding a one-second perturbation at 368,963 s corresponds to the resulting error RMS values.

| ERROR		EKF	AKF	RKF	RAKF
Velocity (m/s)	Eastward	0.0729	0.0478	0.0500	0.0486
	Northward	0.4126	0.0563	0.0570	0.0569
	Upward	0.0993	0.1372	0.0766	0.0666
Attitude (deg)	Pitch	0.3373	0.1283	0.1830	0.1295
	Roll	0.2181	0.1372	0.1930	0.1483
	Heading	0.3893	0.2304	0.3360	0.2359
Position (m)	Eastward	0.0709	0.0510	0.0567	0.0534
	Northward	0.2862	0.0626	0.0667	0.0635
	Upward	0.1835	0.0517	0.0915	0.0701
	3D Accuracy(m)	0.3473	0.0959	0.1266	0.1086
	improved accuracy (%)	68.73%	-	14.22%	

The RMS values of the position, velocity, and attitude errors in the case of 1-s disturbance are shown in Table 9.

Table 9 presents the RMS values of position, velocity, and attitude errors obtained by adding random perturbations within 1 s at GPST 368,963 s. The following conclusions can be drawn from Table 9:

- Regarding position error: When adding 1-s random disturbances ranging from 0 to 1 m, in terms of the East–North–Up (ENU) position error, compared with EKF, the accuracy of RAKF increased by 24.89%, 77.78%, and 68.79%, respectively. Compared to RKF, the accuracy of RAKF achieved improvements of 20.36%, 77.78%, and 68.79%, respectively. Figure 17a–c illustrates the comparison of position errors with 1-s disturbances ranging from 0 to 1 m. In this scenario, the RAKF algorithm outperformed RKF significantly. Compared to EKF and AKF, RAKF demonstrated comparable anti-interference capability but with slightly better performance and closer proximity to 0.

- Regarding velocity error: When adding 1-s random disturbances ranging from 0 to 1 m, in terms of the East–North–Up (ENU) velocity error, compared with EKF, the accuracy of RAKF improved by 31.20%, 86.04%, and 41.88%, respectively. Compared with AKF, the accuracy of RAKF improved by 34.13%, 77.58%, and 7.54%, respectively. Compared with RKF, the speed accuracy of RAKF improved by 29.43%, 79.91%, and 23.30%, respectively.

- Regarding attitude error: When adding 1-s random disturbances ranging from 0 to 1 m, in terms of the pitch, roll, heading, and attitude error, compared with EKF, the accuracy of RAKF improved by 59.38%, 30.15%, and 34.65%, respectively. Compared with AKF, the accuracy of RAKF improved by 14.18%, 7.21%, and 31.53%, respectively. Compared with RKF, the accuracy of RAKF improved by 32.06%, 10.50%, and 18.36%, respectively.

3.3.2. Experimental Results of the Second Group

Within a five-second interval at GPST 369,398 s to 369,402 s, perturbation errors of 0.2721 m, 1.0997 m, 1.1594 m, 0.3380 m, and 0.2899 m were added, and the position, velocity, attitude errors of the four methods were compared. The results are shown in Figure 13. To further analyze the advantages of the four methods under continuous perturbations for five seconds, the position, velocity, and attitude errors were locally magnified during the interval of 369,398 s to 369,402 s, and the comparative results are depicted in Figure 19.
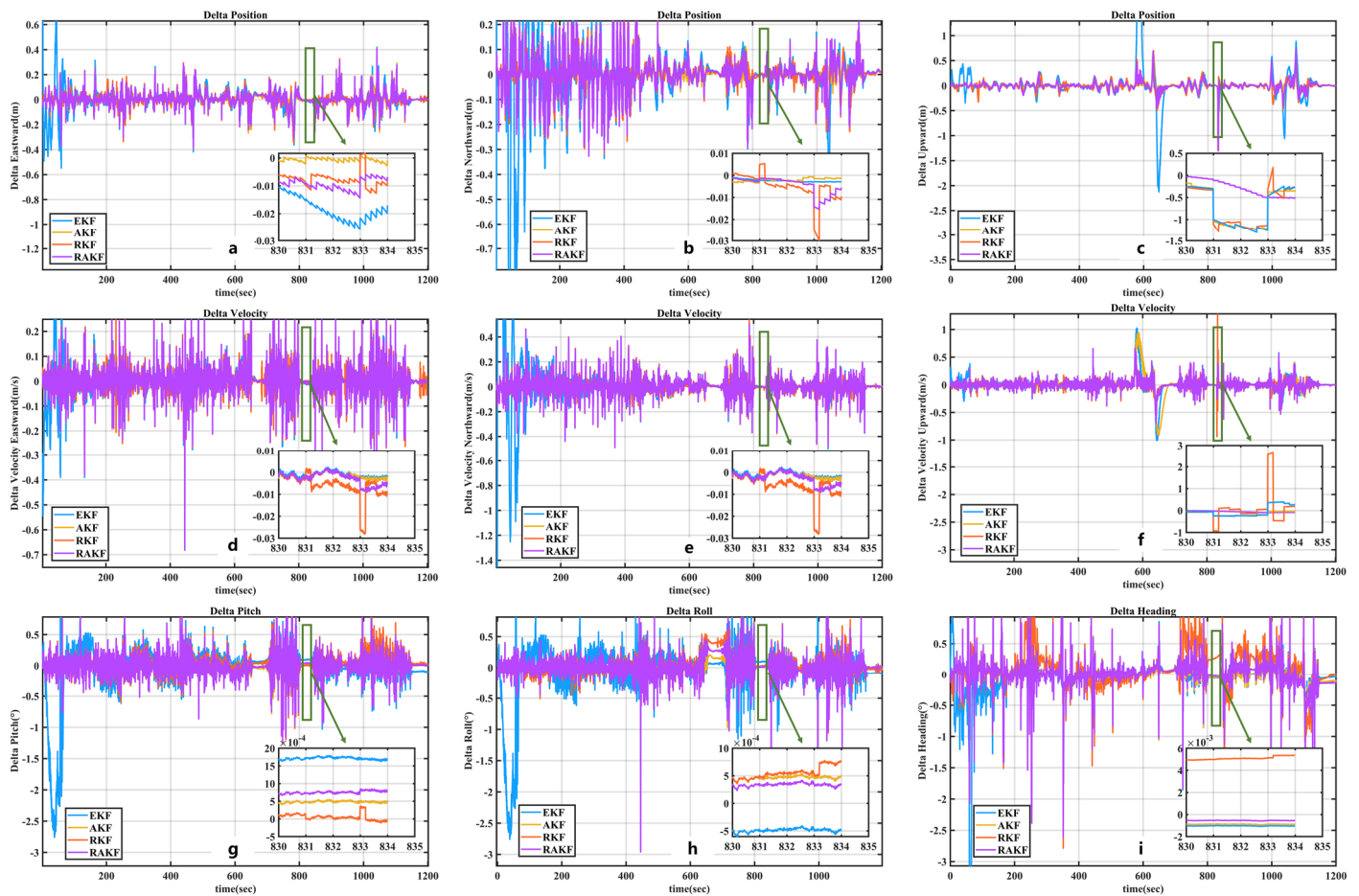
Figure 19. Five-second perturbation position, velocity, and attitude error result diagrams. (**a**) Eastward position error; (**b**) northward position error; (**c**) upward position error; (**d**) eastward velocity error; (**e**) northward velocity error; (**f**) upward velocity error; (**g**) pitch error; (**h**) roll error; (**i**) heading error.

Figure 19 represents the comparison of position, velocity, and attitude error variations under the influence of a 5-s perturbation. The magnified sections show the changes in the four different algorithms with varying degrees of perturbation. In order to further quantify the performance of the four algorithms under continuous perturbations of different magnitudes, the variations in the error RMS histograms are plotted in Figure 20, and the specific RMS values are provided in Table 10.
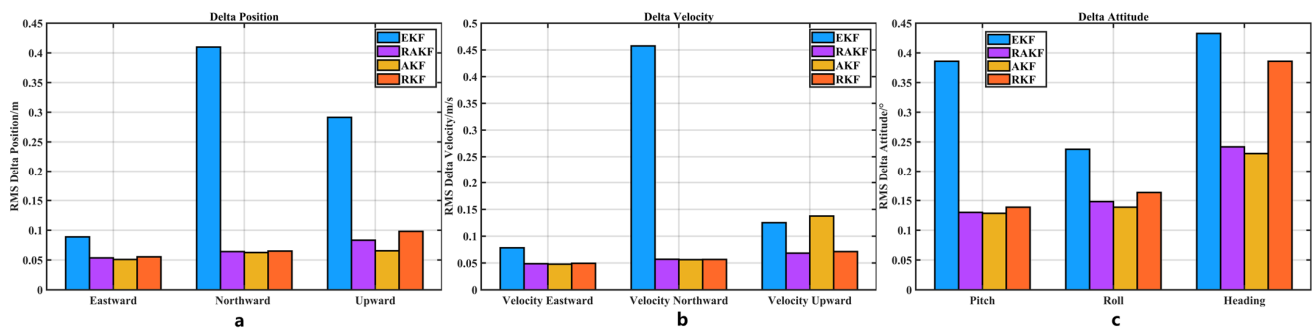
Figure 20. Comparison of RMS values of position, velocity, and attitude errors under 5-s disturbance. (**a**) Position error RMS; (**b**) velocity error RMS; (**c**) attitude error RMS.

Table 10. RMS value of the resultant errors caused by adding 5 s of successive different perturbations at 369,398 s to 369,402 s.

	ERROR	EKF	AKF	RKF	RAKF
Velocity (m/s)	Eastward	0.0782	0.0478	0.0493	0.0486
	Northward	0.4575	0.0563	0.0565	0.0569
	Upward	0.1251	0.1375	0.0712	0.0666
Attitude (deg)	Pitch	0.3858	0.1283	0.1387	0.1295
	Roll	0.2377	0.1386	0.1633	0.1483
	Heading	0.4327	0.2304	0.3858	0.2359
Position (m)	Eastward	0.0889	0.0510	0.0553	0.0534
	Northward	0.4099	0.0626	0.0651	0.0635
	Upward	0.2914	0.0654	0.0981	0.0701
	3D Accuracy(m)	0.5107	0.1039	0.1301	0.1086
	improved accuracy (%)	78.74%	-	16.53%	

Table 10 presents a comparison of the root mean square (RMS) errors in position, velocity, and attitude for the four algorithms under different levels of disturbance for a duration of 5 s. Compared to EKF, RAKF demonstrated significant improvements in the accuracy of position by 39.93%, 84.51%, and 75.94%, respectively. In terms of velocity, RAKF achieved accuracy improvements of 37.85%, 87.56%, and 46.76%, respectively. Furthermore, the precision of pitch, roll, and heading angles showed enhancements of 66.43%, 37.61%, and 45.48%, respectively. Compared to RKF, RAKF exhibited minor improvements in northward and eastward position accuracy but demonstrated a 28.54% improvement in the upward position. While the improvements in northward and eastward velocity were less than 10%, RAKF achieved a 38.85% increase in the accuracy of the heading angle. By analyzing the precision of position, velocity, and attitude under 5 s of disturbance, it is evident that the RAKF algorithm maintains superior stability and reliability compared to the other three algorithms while achieving higher positioning and attitude accuracy.

4. Discussion

In this study, according to the experimental position–velocity error plots, as well as attitude angle error plots in Figures 8 and 9, analyzed from position and attitude angle, the method proposed did not have any obvious advantage over EKF, AKF, and RKF due to the small influence of the perturbation. However, the error results corresponding to different methods changed significantly due to the large influence of anomalous perturbations on the celestial direction velocity. Analyzing the U-direction velocity, the RAKF method shows smaller error changes compared to EKF, AKF, and RKF, and according to Figure 10 and Table 5, the U-direction velocity accuracy improves compared to EKF, AKF, and RKF by 26.44%, 77.58%, and 2.93%, respectively. The stability and anti-interference ability of the RAKF method is better than EKF, AKF, and RKF in the case of abnormal perturbation of onboard data.

In order to further verify the performance of the method, anomalous perturbations of different durations and values were added to the GNSS elevation data, and Figures 11 and 12 show the comparisons of the position velocity, as well as attitude errors, of the four methods in the perturbed case. In the case of perturbation, the performance of the classic anti-differential Kalman filter was greatly affected by the perturbation, mainly because finding a reliable equivalent weight matrix under the perturbation is difficult [37], resulting in an inaccurate setting of the observation noise covariance matrix. The RAKF, AKF, and EKF were less affected by the perturbation, and the RMS values of the different methods are shown in Tables 6 and 7 for the cases of 1-s and 5-s perturbation, respectively. In the case of 1-s perturbation, the 3D position error accuracy of the RAKF method improved by 68.73% and 14.22% compared to the EKF and RKF accuracy, respectively. There was no significant advantage of RAKF positional accuracy over AKF, but RAKF outperformed AKF in attitude and velocity.

When anomalous perturbations frequently occur in the GNSS/INS system processing, the observation noise covariance matrix often adopts a fixed value for representation during data processing [18], which lacks flexibility and is prone to cause dispersion in the combined navigation results. Therefore, constructing an improved observation noise covariance matrix by comprehensively considering the GNSS observation information overcomes the shortcomings of the GNSS positioning error estimation value technique using measures such as variance or standard deviation and has a unique advantage in solving the problem that it is difficult to accurately define the observation noise covariance matrix in terms of a model.

5. Conclusions

In the process of GNSS measurement, accurately describing the measurement noise statistics of GNSS receivers and inertial sensors is difficult due to the influence of various factors, such as complex urban environments. With the aiming of solving this problem, this paper proposed a robust adaptive GNSS/INS integrated navigation method based on an improved measurement noise covariance matrix. The method mainly synthesizes the dynamic measurement noise covariance matrix through the position accuracy factor, the measurement factor, and the position standard deviation, increases the measurement noise covariance matrix when the measurement is abnormally disturbed, and combines robust adaptive filtering to resist the outliers. To assess the performance of this method, the author conducted experiments on land vehicles. The positioning errors of the integrated navigation system using the four solution strategies of the EKF algorithm, AKF algorithm, RKF algorithm, and the proposed method were compared. The experimental results show that compared with the other three algorithms, RAKF has better anti-interference and stability and effectively reduces the influence of abnormal disturbance on GNSS/INS integrated navigation results. In addition, RAKF can better use the position accuracy factor, measurement factor, and position standard deviation in GNSS solution results. And RAKF can overcome the shortcomings of GNSS positioning error estimation technology represented by variance or standard deviation. Limitations of the proposed method still exist. For example, the proposed method only considered the position accuracy factor, measurement factor, and position standard deviation in GNSS measurement results. In the future, the author will consider other prior information to realize the monitoring and isolation of abnormal disturbances. In addition to the monitoring and isolation of abnormal disturbances in vehicle application scenarios, the monitoring and isolation of abnormal disturbances in other application scenarios, such as unmanned ships, is also more important. Therefore, the follow-up to this study will be carried out in the field of navigation and aviation to further test the ability of the algorithm to monitor and isolate abnormal disturbances. And the integrated navigation and positioning results of reliability, accuracy, and stability can be obtained in case of abnormal disturbance.

References

1. Yang, Y.; Yang, C.; Ren, X. PNT intelligent services. *Acta Geod. Et Cartogr. Sin.* **2021**, *50*, 1006–1012. [CrossRef]
2. Yang, Y. Resilient PNT Concept Frame. *Acta Geod. Et Cartogr. Sin.* **2018**, *47*, 893–898. [CrossRef]
3. Filjar, R.; Damas, M.C.; Iliev, T.B. Resilient Satellite Navigation Empowers Modern Science, Economy, and Society. *IOP Conf. Ser. Mater. Sci. Eng.* **2021**, *1032*, 012001. [CrossRef]
4. Fritsche, M.; Sośnica, K.; Rodríguez-Solano, C.J.; Steigenberger, P.; Wang, K.; Dietrich, R.; Dach, R.; Hugentobler, U.; Rothacher, M. Homogeneous Reprocessing of GPS, GLONASS and SLR Observations. *J. Geod.* **2014**, *88*, 625–642. [CrossRef]
5. Zhang, B.; Hou, P.; Zha, J.; Liu, T. Integer-Estimable FDMA Model as an Enabler of GLONASS PPP-RTK. *J. Geod.* **2021**, *95*, 91. [CrossRef]
6. Paziewski, J.; Wielgosz, P. Assessment of GPS + Galileo and Multi-Frequency Galileo Single-Epoch Precise Positioning with Network Corrections. *GPS Solut.* **2014**, *18*, 571–579. [CrossRef]
7. Qu, L.; Du, M.; Wang, J.; Gao, Y.; Zhao, Q.; Zhang, Q.; Guo, X. Precise Point Positioning Ambiguity Resolution by Integrating BDS-3e into BDS-2 and GPS. *GPS Solut.* **2019**, *23*, 63. [CrossRef]
8. Chai, D.; Sang, W.; Chen, G.; Ning, Y.; Xing, J.; Yu, M.; Wang, S. A Novel Method of Ambiguity Resolution and Cycle Slip Processing for Single-Frequency GNSS/INS Tightly Coupled Integration System. *Adv. Space Res.* **2022**, *69*, 359–375. [CrossRef]
9. Hu, L.; Bao, Y.; Sun, Z.; Meng, X.; Tang, C.; Zhang, D. Outlier Detection Based on Nelder-Mead Simplex Robust Kalman Filtering for Trustworthy Bridge Structural Health Monitoring. *Remote Sens.* **2023**, *15*, 2385. [CrossRef]
10. Feng, S.; Ochieng, W.; Moore, T.; Hill, C.; Hide, C. Carrier Phase-Based Integrity Monitoring for High-Accuracy Positioning. *GPS Solut.* **2009**, *13*, 13–22. [CrossRef]
11. Jiang, C.; Zhao, D.; Zhang, Q.; Liu, W. A Multi-GNSS/IMU Data Fusion Algorithm Based on the Mixed Norms for Land Vehicle Applications. *Remote Sens.* **2023**, *15*, 2439. [CrossRef]
12. Cheng, S.; Cheng, J.; Zang, N.; Cai, J.; Fan, S.; Zhang, Z.; Song, H. Adaptive Non-Holonomic Constraint Aiding Multi-GNSS PPP/INS Tightly Coupled Navigation in the Urban Environment. *GPS Solut.* **2023**, *27*, 152. [CrossRef]
13. Chai, D.; Chen, G.; Wang, S.; Lu, X. Loosely Coupled GNSS/INS Integration Based on an Auto Regressive Model in a Data Gap Environment. *Acta Geod. Geophys.* **2018**, *53*, 691–715. [CrossRef]
14. Xiao, Y.; Luo, H.; Zhao, F.; Wu, F.; Gao, X.; Wang, Q.; Cui, L. Residual Attention Network-Based Confidence Estimation Algorithm for Non-Holonomic Constraint in GNSS/INS Integrated Navigation System. *IEEE Trans. Veh. Technol.* **2021**, *70*, 11404–11418. [CrossRef]
15. Musoff, H.; Zarchan, P. *Fundamentals of Kalman Filtering: A Practical Approach*, 3rd ed.; American Institute of Aeronautics and Astronautics: Reston, VA, USA, 2009; ISBN 978-1-60086-718-7.
16. Zhang, B.; Hou, P.; Liu, T.; Yuan, Y. A Single-Receiver Geometry-Free Approach to Stochastic Modeling of Multi-Frequency GNSS Observables. *J. Geod.* **2020**, *94*, 37. [CrossRef]
17. Chen, G. Introduction to random signals and applied Kalman filtering, 2nd edn. Robert Grover Brown and Patrick Y. C. Hwang, Wiley, New York, 1992. ISBN 0-471-52573-1, 512 pp., $62.95. *Int. J. Adapt. Control. Signal Process.* **1992**, *6*, 516–518. [CrossRef]
18. Ding, W.; Wang, J.; Rizos, C.; Kinlyside, D. Improving Adaptive Kalman Estimation in GPS/INS Integration. *J. Navig.* **2007**, *60*, 517–529. [CrossRef]
19. Yan, W.; Bastos, L.; Gonçalves, J.A.; Magalhães, A.; Xu, T. Image-Aided Platform Orientation Determination with a GNSS/Low-Cost IMU System Using Robust-Adaptive Kalman Filter. *GPS Solut.* **2018**, *22*, 12. [CrossRef]

20. Liu, S.; Wang, K.; Abel, D. Robust State and Protection-Level Estimation within Tightly Coupled GNSS/INS Navigation System. *GPS Solut.* **2023**, *27*, 111. [CrossRef]

21. Huang, Y.; Zhang, Y.; Wu, Z.; Li, N.; Chambers, J. A Novel Adaptive Kalman Filter With Inaccurate Process and Measurement Noise Covariance Matrices. *IEEE Trans. Automat. Contr.* **2018**, *63*, 594–601. [CrossRef]

22. Mohamed, A.H.; Schwarz, K.P. Adaptive Kalman Filtering for INS/GPS. *J. Geod.* **1999**, *73*, 193–203. [CrossRef]

23. Wang, J. Stochastic Modeling for Real-Time Kinematic GPS/GLONASS Positioning. *Navigation* **1999**, *46*, 297–305. [CrossRef]

24. Hide, C.; Moore, T.; Smith, M. Adaptive Kalman Filtering for Low-Cost INS/GPS. *J. Navig.* **2003**, *56*, 143–152. [CrossRef]

25. Meng, Y.; Gao, S.; Zhong, Y.; Hu, G.; Subic, A. Covariance Matching Based Adaptive Unscented Kalman Filter for Direct Filtering in INS/GNSS Integration. *Acta Astronaut.* **2016**, *120*, 171–181. [CrossRef]

26. Yang, Y.; He, H.; Xu, G. Adaptively Robust Filtering for Kinematic Geodetic Positioning. *J. Geod.* **2001**, *75*, 109–116. [CrossRef]

27. Gao, S.; Zhong, Y.; Li, W. Robust Adaptive Filtering Method for SINS/SAR Integrated Navigation System. *Aerosp. Sci. Technol.* **2011**, *15*, 425–430. [CrossRef]

28. Niu, X.; Wu, J.; Zhang, Q. Research on Measurement Error Model of GNSS/INS Integration Based on Consistency Analysis. *Gyroscopy Navig.* **2018**, *9*, 243–254. [CrossRef]

29. Niu, X.; Dai, Y.; Liu, T.; Chen, Q.; Zhang, Q. Feature-Based GNSS Positioning Error Consistency Optimization for GNSS/INS Integrated System. *GPS Solut.* **2023**, *27*, 89. [CrossRef]

30. Crespillo, O.G.; Medina, D.; Skaloud, J.; Meurer, M. Tightly coupled GNSS/INS integration based on Robust M-Estimators. In Proceedings of the 2018 IEEE/ION Position, Location and Navigation Symposium (PLANS), Portland, OR, USA, 20–23 April 2020; IEEE: Monterey, CA, USA; pp. 1554–1561.

31. Yang, Y. *Adaptive Dynamic Navigation and Positioning*; Surveying and Mapping Press: Beijing, China, 2017; ISBN 978-7-5030-4005-4.

32. Mao, Y.; Sun, R.; Wang, J.; Cheng, Q.; Kiong, L.C.; Ochieng, W.Y. New Time-Differenced Carrier Phase Approach to GNSS/INS Integration. *GPS Solut.* **2022**, *26*, 122. [CrossRef]

33. Wen, W.; Kan, Y.C.; Hsu, L.-T. Performance comparison of GNSS/INS integrations based on EKF and factor graph optimization. In Proceedings of the 32nd International Technical Meeting of the Satellite Division of The Institute of Navigation (ION GNSS+ 2019), Miami, FL, USA, 16–20 September 2019; pp. 3019–3032.

34. Yan, G.; Weng, J. *Integrated Inertial Navigation Algorithms and Principles of Integrated Navigation*; Northwestern Polytechnical University: Xi'an, China, 2019; ISBN 978-7-5612-6547-5.

35. Jiang, C. Filtering algorithms and reliability analysis for GNSS/INS integrated navigation systems. *Acta Geod. Et Cartogr. Sin.* **2020**, *49*, 1376. [CrossRef]

36. Yang, Y.; Ren, X.; Xu, Y. Main Process of Adaptively Robust Filter with Applications in Navigation. *J. Navig. Position.* **2013**, *1*, 9–15. [CrossRef]

37. Jiang, C.; Zhang, S.; Li, H.; Li, Z. Performance Evaluation of the Filters with Adaptive Factor and Fading Factor for GNSS/INS Integrated Systems. *GPS Solut.* **2021**, *25*, 130. [CrossRef]

38. Knight, N.L.; Wang, J. A Comparison of Outlier Detection Procedures and Robust Estimation Methods in GPS Positioning. *J. Navig.* **2009**, *62*, 699–709. [CrossRef]

39. Niu, Z.; Li, G.; Guo, F.; Shuai, Q.; Zhu, B. An Algorithm to Assist the Robust Filter for Tightly Coupled RTK/INS Navigation System. *Remote Sens.* **2022**, *14*, 2449. [CrossRef]

40. Akhlaghi, S.; Zhou, N.; Huang, Z. Adaptive adjustment of noise covariance in Kalman filter for dynamic state estimation. In Proceedings of the IEEE Power Energy Society General Meeting, Chicago, IL, USA, 16–20 July 2017; pp. 1–5. [CrossRef]